ORIGINAL ARTICLE

Evolution of blast wave profiles in simulated air blasts: experiment and computational modeling

**N. Chandra · S. Ganpule · N. N. Kleinschmit ·
R. Feng · A. D. Holmberg · A. Sundaramurthy ·
V. Selvan · A. Alai**

Abstract Shock tubes have been extensively used in the study of blast traumatic brain injury due to increased incidence of blast-induced neurotrauma in Iraq and Afghanistan conflicts. One of the important aspects in these studies is how to best replicate the field conditions in the laboratory which relies on reproducing blast wave profiles. Evolution of the blast wave profiles along the length of the compression-driven air shock tube is studied using experiments and numerical simulations with emphasis on the shape and magnitude of pressure time profiles. In order to measure dynamic pressures of the blast, a series of sensors are mounted on a cylindrical specimen normal to the flow direction. Our results indicate that the blast wave loading is significantly different for locations inside and outside of the shock tube. Pressure profiles inside the shock tube follow the Friedlander waveform fairly well. Upon approaching exit of the shock tube, an expansion wave released from the shock tube edges significantly degrades the pressure profiles. For tests outside the shock tube, peak pressure and total impulse reduce drastically as we move away from the exit and majority of loading is in the form of subsonic jet wind. In addition, the planarity of the blast wave degrades as blast wave evolves three dimensionally. Numerical results visually and quantitatively confirm the presence of vortices, jet wind and three-dimensional expansion of the planar blast wave near the exit. Pressure profiles at 90° orientation show flow separation. When cylinder is placed inside, this flow separation is not sustained, but when placed outside the shock tube this flow separation

is sustained which causes tensile loading on the sides of the cylinder. Friedlander waves formed due to field explosives in the intermediate-to far-field ranges are replicated in a narrow test region located deep inside the shock tube.

1 Introduction

Due to the increased use of improvised explosive devices (IED's) in military conflicts, there has been a major increase in the number of traumatic brain injuries (TBI's) [1]. A major limitation of the current state of blast-induced TBI (BTBI) is the paucity of information on the pathophysiology of blast-induced neurotrauma (BINT) [2]. This has led to an increase in blast studies in recent years through animal models, head surrogates and human cadavers using shock tubes [3–15]. In this work the attention is focused on compressed gas (e.g. Helium, Nitrogen) driven air shock tubes, which are extensively used as the standard research tool. The energy to drive the air shock can also be obtained from small explosives [4,16] as well as combustible fluids like oxy-acetylene [17]. While explosives yield higher overpressures, the test specimens will be subjected to smoke and chemical residues. The combustible shock tubes can easily generate high pressures with less kinetic energy; however, varying both overpressure and duration independently is a challenge. In all these research efforts, the effect of sample placement (or discussion of consideration of sample placement) along the length of the shock tube is not critically analyzed. The locations include placement of the sample at various locations inside and outside of the shock tube. Placement of the sample outside the

N. Chandra (✉) · S. Ganpule · N. N. Kleinschmit · R. Feng ·
A. D. Holmberg · A. Sundaramurthy · V. Selvan · A. Alai
Department of Mechanical and Materials Engineering,
University of Nebraska-Lincoln, Lincoln, NE 68588-0656, USA
e-mail: nchandra2@unl.edu
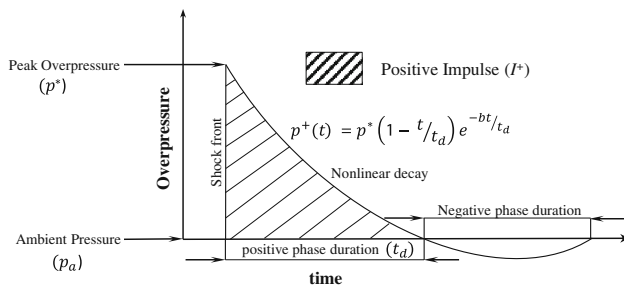
Fig. 1 Mathematical representation of planar Friedlander waveform. Equation in the figure represents instantaneous overpressure p^+ at given time t, where p^* is the peak overpressure, t_d is positive phase duration and b is decay constant

shock tube is preferred by researchers, as the dimensions of the sample are equivalent or larger than the cross-sectional dimensions of the shock tube [9,15]. It is known that the pressure profiles continuously change along the length of the shock tube [18], which in turn can change biomechanical response of the sample (e.g. animal, cadaver) in terms of injury type, severity and lethality. Thus to create an accurate representation of a blast wave generated from an IED in the far-field range, the sample placement must be carefully considered. The goal of this work was to understand blast wave evolution along the length of the shock tube with particular emphasis on the evolution when blast wave exits the shock tube.

In a typical free-field explosion, a blast wave propagates radially from the source of the explosive. Close to the source of the explosion, the pressure history is very turbulent and unpredictable, but further away from the center the blast wave takes the form of a Friedlander wave [19]. This wave has the characteristics of shock front followed by nonlinear decay as shown in Fig. 1. In this work we focus on Friedlander wave (positive phase) implicated in BINT.

2 Review of shock tube theory

Although individual shock tubes for blast wave simulation may have different features for different purposes, the essential wave physics can be understood by analyzing the wave propagation in a generic shock tube configuration as shown in Fig. 3. A typical (compression driven) shock tube consists of a driver section of pressurized gas and a driven section of air at atmospheric pressure with the two sections separated by set of membranes. When the membranes bursts, the driver gas expands rapidly and compresses the atmospheric air (i.e. driven gas) in front to a shocked state, which propagates forward as an air shock wave. Meanwhile, the driver gas expansion initiates a family of infinite rarefaction waves (expansion fan). These rarefaction waves first travel towards closed end, get reflected at the closed end and then travel

towards open end. Their sequential arrivals at a given location of driven section produce a nonlinear decay (see wave profiles a–c of Fig. 2). The wave profile evolves with propagation distance to that of a Friedlander wave (curve c of Fig. 2) when the fastest rarefaction wave (which is faster than the shock front) catches the shock front at $x = x^*$, where the shock front intensity is eroded the least by the rarefaction waves. Hence, at $x = x^*$, peak overpressure p^* has the maximum value with a Friedlander wave profile. The time for the nonlinear decay to reach $p = 0$ gives overpressure duration t^*, which has the minimum value at $x = x^*$. Before the initial catch-up, $x < x^*$ (curves a and b of Fig. 2) the blast wave assumes a flat-top shape as rarefaction wave reflected from the closed end has not reached yet. The flat-top duration is given by the difference in the arrival times of the shock front and the fastest rarefaction wave. In the range $x^* < x < 0$ where $x = 0$ represents the shock tube exit, more and more rarefaction waves catch up the shock front causing decreasing p^* and increasing t^* with increasing x. The pressure–time (p–t) profile near (outside) the exit is shown by curve d of Fig. 2; notice that the waveform is changed significantly (low p^*, low t^*, followed by jet wind).

Studies on evolution of the shock wave at the exit or open end have attracted researchers over the years, due to numerous flow phenomena occurring at the exit [20–26]. It is shown in these studies that at the exit of the shock tube, the shock wave evolves from planar to three-dimensional spherical with other effects like vortex formation, secondary shock formation, Mach disc, subsonic jet flow, shock-vortex interaction and impulsive noise. All of the aforementioned effects may or may not been seen depending on the shock wave strength and geometry of the exit. Most of these studies, however, have focused on flow dynamics aspects with no emphasis on qualitative or quantitative analysis of shock/blast wave profiles (e.g. pressure–time (p–t) profiles). This becomes particularly important when one wants to use shock tube to generate desired dynamic mechanical load both in terms of shape and magnitude. The present work focuses on the shape and magnitude aspect of pressure time profile (referred as pressure profile/(s) from here on) of blast wave along the length of the shock tube, both inside and outside from the exit (open end). Such studies of blast waves are important in the basic understanding of shock/blast wave dynamics and in engineering applications (e.g. in the study of blast-structure or blast-human interactions) as well.

3 Materials and methods

3.1 Experiments

The shock tube used to generate the blast waves for this study is located at the University of Nebraska-Lincoln's blast wave

Fig. 2 Evolution of shock wave in a generic shock tube
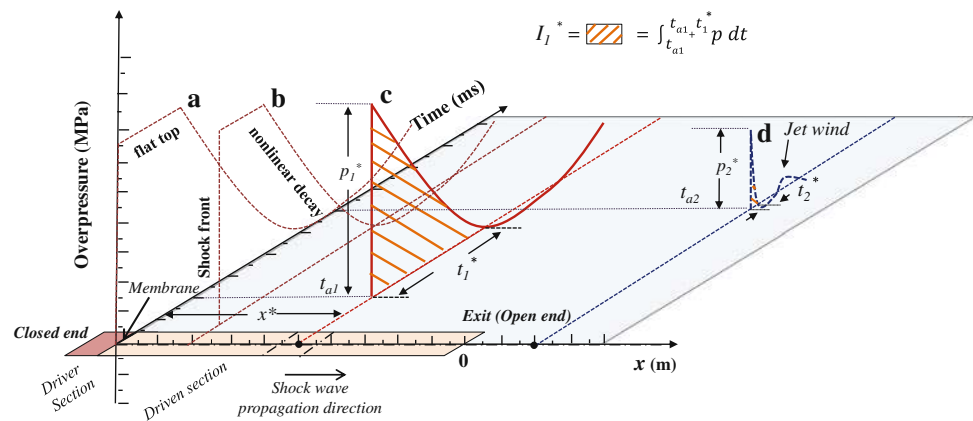
generation facility [27]. The three main components of the shock tube are the driver, transition and driven sections. The circle-to-square transition is used to change the cross-section of the tube from a circular cylinder (driver section) to a square (driven sections); the square section is a design element to observe events in the test section (which is part of driven section) with high-speed video imaging (600,000 frames/s). The length and diameter of the driver section is 295 mm and 101 mm, respectively. The transition is composed of 6.35-mm-thick hot rolled steel. It was brake-formed in two pieces and welded together. It has a 5.9° taper from the driver to the driven section. This angle is selected so as to minimize turbulence caused by boundary layer separation as the driver is discharged. The driven section has a cross section of 230 mm × 230 mm and the length of 6225 mm (Fig. 3a).

The unique features of UNL shock tube lies in its ability to produce a range of peak overpressures, durations and impulses that can all be independently controlled within reasonable limits. These are achieved by having variable driver length, placing the test specimens at many selected locations along the driven section (with the ability to capture live videos) and an end plate modifier that can alter the wave profiles. Further wave tailoring is also achieved using different driver gases and burst pressures (by altering the thickness of the membranes). The working fluid is always air, as the driven gas stays well within a few diameter of the driver. Though the pressure–time profile in this work emphasizes all positive pressures, experiments with negative pressures have been obtained by changing gas pressure, transitions and specimen placements.

In addition to the aforementioned, the generation of shock-blast wave profile is affected by a number of tube parameters; length and diameter of the driver; length and diameter of the driven; transition section if the driver and driven are of different shape or size; type of driver and driven fluids and their pressures. In order to obtain higher peak overpressures, one can either increase the burst pressure, or use Helium instead

of Nitrogen or air, heat the driver gas or reduce the pressure in the driven section to partial vacuum. Further, when the diameter of the driven is increased higher driver volume of gas at high pressure is required to reach the same peak overpressure profile. As the driver dimension increases, the location of optimal test location changes based on the driver gas, driver pressure and the transition design. As the peak overpressure decreases and duration increases downstream of optimal test location, having a longer length leads to lower peak overpressure and longer duration; however, if the length is too short, then the shock is not fully developed (the rarefaction wave from the driver has not reached the leading edge of the shock) the shock assumes a flat-topped wave shape.

In the patented UNL design, pure pressurized nitrogen was used as the driver gas, and the driven gas was air at ambient laboratory conditions (temperature range of 23 ± 2 °C). The evolution of the blast wave along the length of the shock tube was measured using an aluminum cylinder (length = 230 mm and diameter = 41.3 mm). In order to measure the evolution of blast wave along the length of the shock tube, the cylinder was placed along the longitudinal axis of the shock tube at various offset distances from the exit (open end) both outside ($+x$) and inside ($-x$) (Fig. 3b). Seven holes were drilled and tapped to locate seven Dytran model 2300V1 piezoelectric pressure sensors used in conjunction with Dytran model 6502 mounting adapters. The location labeled t0 was centered between the two end surfaces of the cylinder, and the rest of the holes were evenly spaced for a total span of 84 mm (Fig. 3b). The cylinder was mounted (i.e. firmly secured) using brackets made out of flat steel bar. In addition to the gauges mounted on the cylinder there were set of gauges (PCB pressure sensor model 134A24) mounted at various locations on the shock tube (along the length) which measure the incident (side-on) pressures (Fig. 3a). Experiment was repeated three times at each location along the length of the shock tube ($N = 3$).

Fig. 3 a Photographs of 230 mm × 230 mm square shock tube used in this work. **b** Experimental setup to measure evolution of the shock wave along the length of the shock tube. Placement of the cylinder at two representative locations along the length of the shock tube is shown
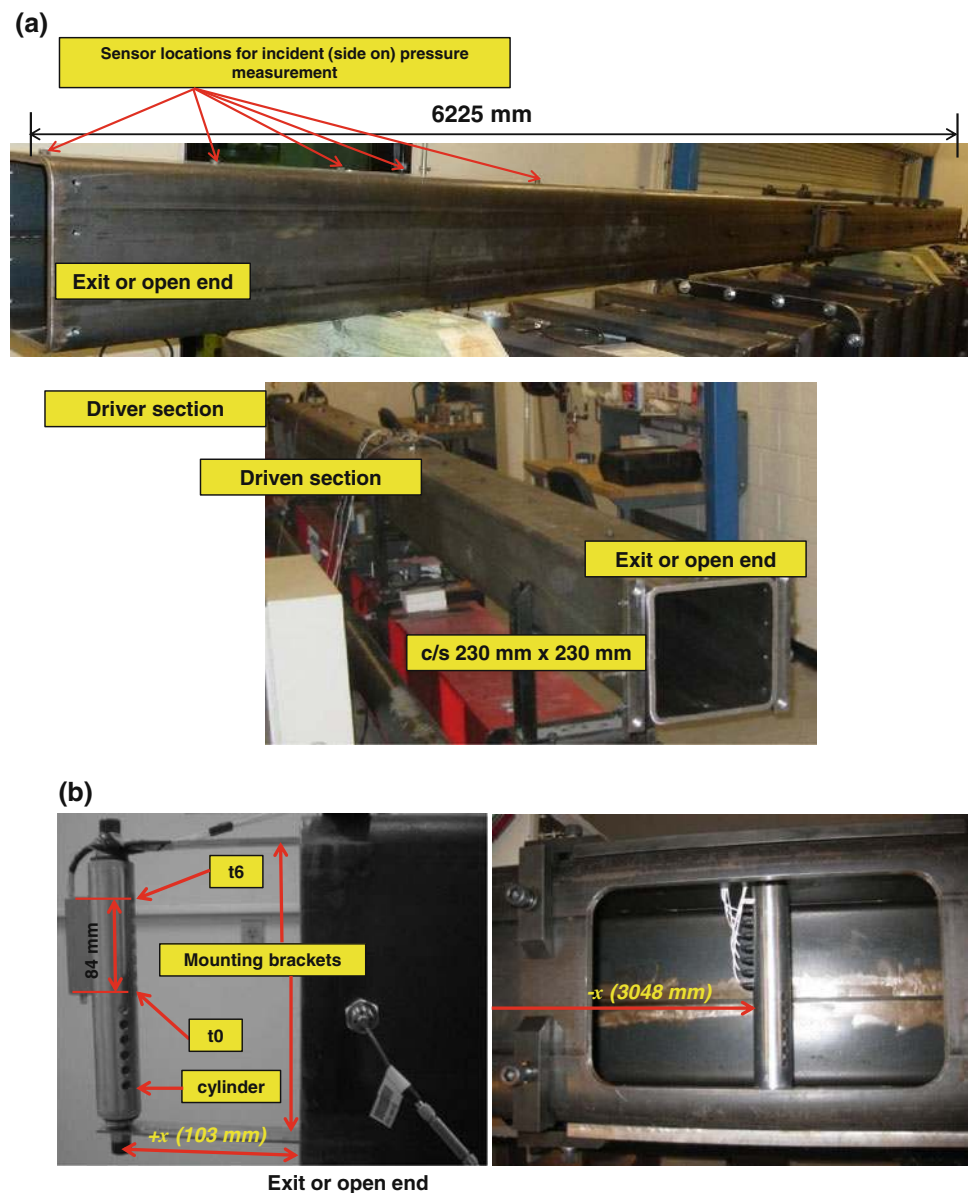
3.2 Computational modeling

Finite element (FE) based numerical approach is used to depict the experiments and to simulate the flow inside and outside of the shock tube. The numerical techniques like finite element method (FEM) and computational fluid dynamics (CFD) were effectively used to study flow fields at the exit of the shock tube in the past [21–23,28]. The main goal of the numerical simulation(s) in this work is to understand the flow field as the blast wave exits the open end of the square shock tube. The effect is seen not only outside but also inside the tube. Simulations are carried with cylinder placed at various locations inside and outside of the shock tube. An additional simulation is carried out without the cylinder to understand mechanics of the undisturbed flow field.

3.2.1 FE discretization

In our FE modeling, the blast wave propagation and its interaction with the cylinder are treated as fluid structure interaction (FSI) problem. The air inside and outside of the shock tube is modeled as Eulerian elements and the cylinder and mounting bracket are modeled as Lagrangian elements. Eulerian framework allows for the modeling of highly dynamic events (e.g. shock) which would otherwise induce heavy mesh distortion. The size of the Eulerian domain is 7000 × 5000 × 5000 mm^3. The size of the Eulerian domain is selected such that the reflections from domain boundaries are negligible during total simulation time of interest. This Eulerian domain is meshed with 7,016,115 hexahedral elements. Biased meshing is used to reduce the total number of

Fig. 4 Simulation setup. Cut view in transverse plane
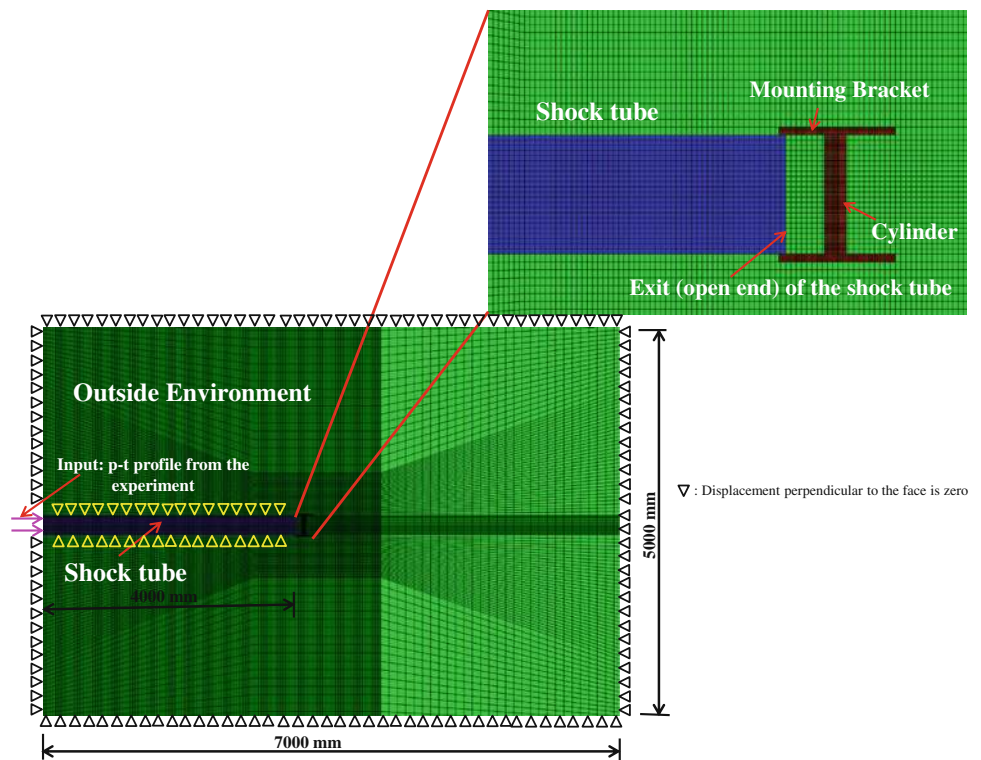
elements. The cylinder and mounting brackets are meshed to generate 23,948 hexahedral elements. The experimental pressure boundary condition (i.e. experimentally measured pressure–time (p–t) profile deep inside the shock tube) is used as an input for the FE simulations. Figure 4 shows the simulation setup (2D section in transverse plane is shown for simplicity). The displacement perpendicular to each face of the shock tube is kept zero to avoid escaping/leaking of air through these faces. This will maintain a planar shock front traveling in the longitudinal direction with no lateral flow. In addition, displacement perpendicular to the external boundaries of Eulerian domain is also kept zero to avoid escaping/leaking of air through these faces. The tied constraint is used between open end of the shock tube and mounting brackets and cylinder and mounting brackets.

3.2.2 Material models

Air is modeled as an ideal gas equation of state (EOS). The Mach number of the shock front from our experiments is approximately 1.5; hence the ideal gas EOS assumption is acceptable, as the ratio of specific heats do not change drastically at this Mach number. Cylinder and mounting brackets are modeled as linear, elastic, isotropic solids.

3.2.3 Solution scheme

The finite element model is solved using nonlinear transient dynamic procedure with Euler–Lagrangian coupling method

(Abaqus®). In this procedure, the governing partial differential equations for the conservation of momentum, mass and energy along with the material constitutive equations and the equations defining the initial and the boundary conditions are solved simultaneously. An enhanced immersed boundary method is used to provide the coupling between the Eulerian and the Lagrangian domains. Here, the Lagrangian region resides fully or partially within the Eulerian region and provides *no-flow* boundary conditions to the fluid in the direction normal to the local surface. Further, the Eulerian region provides the pressure boundary conditions to the Lagrangian region. Thus, a combination of fixed Eulerian mesh and solid–fluid interface modeling through the enhanced immersed boundary method allows for the concurrent simulations of the formation and propagation of a primary blast wave in a fluid medium and accounts for the aerodynamic effects once the blast wave encounters a solid. A typical simulation required about 2 h of CPU time, run on a dedicated 64 Opteron parallel processors (processor speed 2.2 GHz, 2 GB memory per processor) for an integration time of 20 ms.

4 Results and discussion

All experimental results presented in this work are for sensor t0, 0° orientation (unless stated otherwise) and are based on average over three shots ($N = 3$) for each placement location. The experimental conditions were selected so that the pressure–time profiles remain positive (all compressive).

Fig. 5 a Experimentally measured *p–t* profiles at various *x* locations inside the shock tube. *p–t* profiles follow Friedlander waveform fairly well. **b** Experimentally measured *p–t* profiles at various *x* locations outside the shock tube. In these profiles the trends do not follow Friedlander waveform and peak overpressure drastically reduces as we move away from the exit. The starting points of subsonic jet wind are demarcated by *cross symbols*
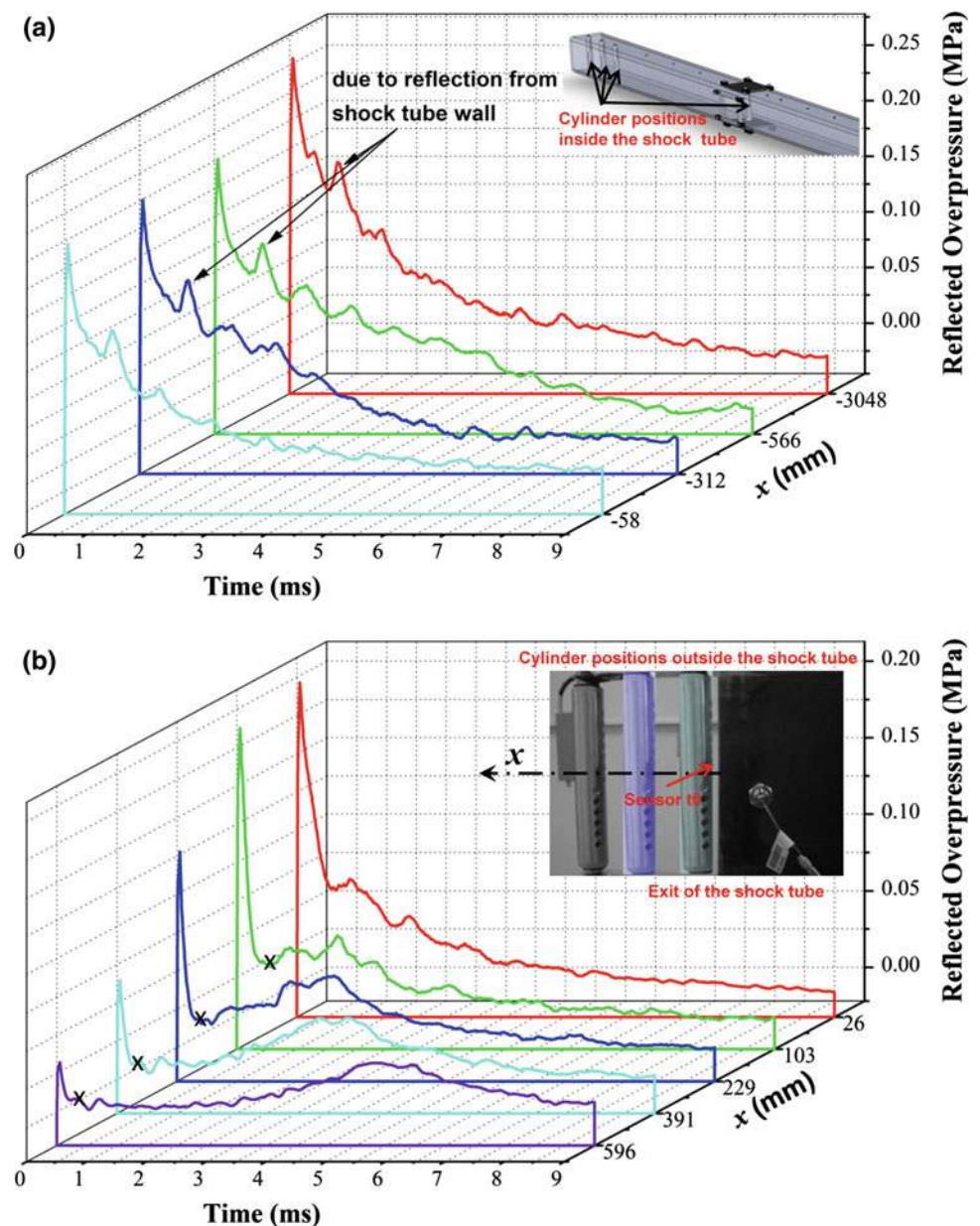
However, the shock tube is capable of producing negative pressure by selecting shorter driver length and locating specimens close to the driver; the negative pressure effect can be a factor in BTBI and will be studied in the future. In the current experiments, each shot is well controlled and the experimental measurements are repeatable with only slight variation (<5 %) in peak-to-peak variation in blast overpressures. Arrival of a shock wave at sensor t0 is set as $t = 0$ for each placement location.

4.1 Pressure and impulse profiles along the length of the shock tube

Figure 5a, b, respectively, shows the reflected pressure profiles for cylinder placement locations inside and outside

of the shock tube. The reflected pressure measures total pressure (both kinetic and potential energy components) at a given point. The reflected pressure profiles for placement locations inside the shock tube show the gradual decay in pressure and pressure profiles follow the Friedlander waveform. Small secondary peak in pressure profiles is due to reflection from walls of the shock tube; however, these wall reflections do not significantly affect pressure profiles. The reflected pressure profiles for placement locations outside the shock tube show rapid pressure decay. Pressure profiles do not conform to the Friedlander waveform; shock front and pressure decay rather look like delta function. This is followed by long duration, relatively constant low-pressure regime (starting points of which are demarcated by cross symbols). This long duration,
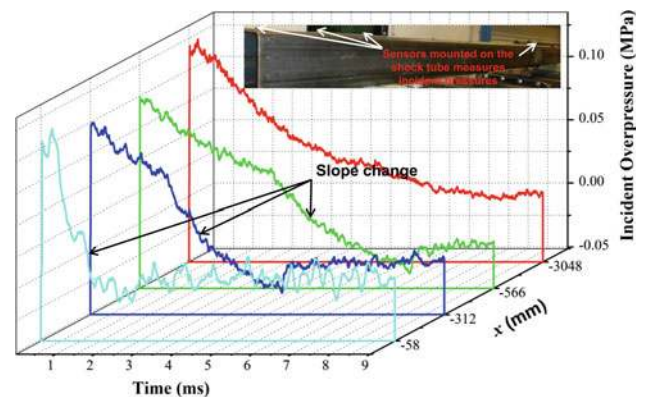
(a)

(b)
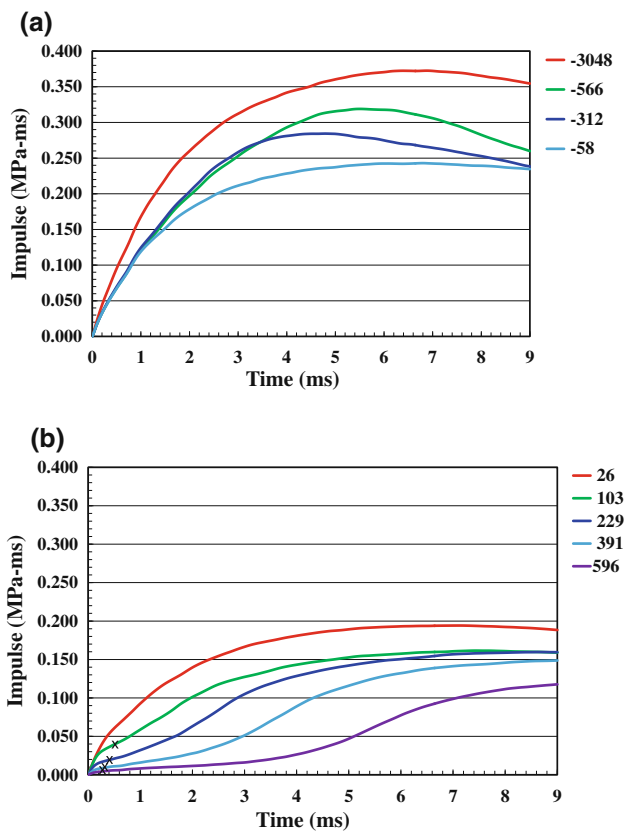
Fig. 6 **a** Impulse profiles at various x locations inside the shock tube obtained by integration of experimentally measured p–t profiles. **b** Impulse profiles at various x locations outside the shock tube obtained by integration of experimentally measured p–t profiles. Contribution of the subsonic jet wind to the impulse is demarcated by *cross symbols*

Fig. 7 Experimentally measured incident (side-on) p–t profiles at various x locations inside the shock tube. Note the slope change for locations near the exit due to rarefaction wave

relatively constant low-pressure regime is referred as subsonic jet wind in this work. This jet wind is an artifact of the shock tube exit effect and does not occur in free-field blast conditions.

Figure 6a, b, respectively, shows the impulse profiles for cylinder placement locations inside and outside of the shock tube. The total impulse is reduced significantly for outside placement locations when compared with inside placement locations. The shape of impulse profiles for placement locations inside the shock tube is relatively constant (i.e. gradual increase) as opposed to non-gradual (i.e. with slope changes) for outside placement locations. The contribution of subsonic jet wind to the impulse is high (starting points of which are demarcated with cross symbols in Fig. 5b).

Figure 7 shows the incident (or side-on) pressure profiles for locations inside the shock tube. These locations are similar to the one presented in Fig. 5a, the only difference being the cylinder was not present during these measurements. The incident pressure measures only potential energy component and does not take into account kinetic energy part; thus peak incident pressures will always be lower than peak reflected pressures. The incident (Fig. 7) and reflected

(Fig. 5a) pressure profiles for these locations are similar qualitatively, except that there is change in slope (during nonlinear decay) in incident pressure profiles of Fig. 7 for locations close to the exit. This change in slope is due to the rarefaction wave from the exit (open end) of the tube moving into the tube. The reflected pressure profiles do not show the change in slope because the cylinder measurements are carried out with sensors facing the blast and dynamic effects produced by dimensions of the cylinder that might block the rarefaction wave reaching the blast-facing sensors. Due to these effects sensors facing the blast do not record rarefaction wave. If we rotate the cylinder by 180° in the experiments (wherein the sensors will face the rarefaction wave), then sensors will record the rarefaction wave. Numerical simulations have confirmed these observations (results not shown for brevity). Thus while conducting testing just inside the shock tube (from open end) one needs to be aware of this rarefaction wave from the exit (open end) moving back into the tube as it may change the loading history.

4.2 Planarity of the blast wave

Figure 8 shows normalized arrival times for sensors t0 through t6 for cylinder placement locations outside the shock tube. Arrival times are normalized with respect to sensor t0. Difference in arrival time indicates non-planarity of the blast wave. It can be seen that, upon exiting the shock tube blast wave is planar till distance (offset) of 75 mm, after this distance blast wave becomes progressively non-planar until peaking at an offset of 307 mm. After the offset of 307 mm the non-planarity starts to decrease and eventually at farther distances it will become planar again but at the cost of decreased pressures (Fig. 5b). A number of tests to check planarity inside the shock tube were also conducted (detailed not shown here); they all show that planarity is maintained within the tube [29].
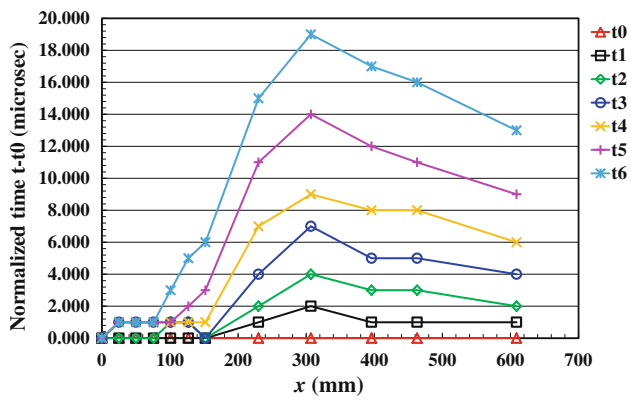
Fig. 8 Normalized arrival times of the blast wave for sensors t0 through t6 as a function of distance from the exit of the shock tube

Planarity is an important feature of the open-field blast waves in the intermediate- to far-field range for BINT studies; as the sizes of wave front are much larger than that of a human body (i.e. larger radius of curvature with respect to human body). The interactions of such a blast wave with a human body are influenced strongly by the confinement of an effectively edgeless wave front. This characteristic must be recreated in a testing to realistically simulate free-field blast loading. As a spherical wave, the strain associated with the blast wave is actually triaxial. The circumferential strain component is given by d/r with d being the particle displacement and r being distance from source of explosion, thus decreasing with increasing r. For a blast wave with a shock front speed up to Mach 2 (twice the sound speed = 686 m/s) at an ambient temperature of 20 °C, the particle velocity jump across the shock front is less than 429 m/s, the associated d less than 0.5 mm and the associated circumferential strain component less than 10^{-4} for r beyond 5 m. Compared with 37.5 % specific volume reduction (98 % true compressive volume strain) across the front of a Mach 2 air shock wave, the circumferential strain component ($<10^{-4}$) is negligible. Therefore, a blast wave in the intermediate to far range can be well approximated with a (uniaxial-strain) planar Friedlander wave.

Planarity of the shock-blast wave will be affected by the very presence of test specimens due to flow obstructions. In order to maintain acceptable levels, the ratio of the projected area of the specimen to that of the shock tube cross-sectional area should be maintained below a critical level. It was found that when the specimen occupies less than 50 % of the area inside the shock tube, the shock wave structure and the measured pressure profiles on the surface of the specimen are relatively unaffected. Further, the pressure differential across the specimen (anterior-posterior direction) is minimal as the shock wave quickly engulfs the specimen, as measured by the negligible rigid body acceleration of specimen (e.g. anthropometric dummy head) [10].
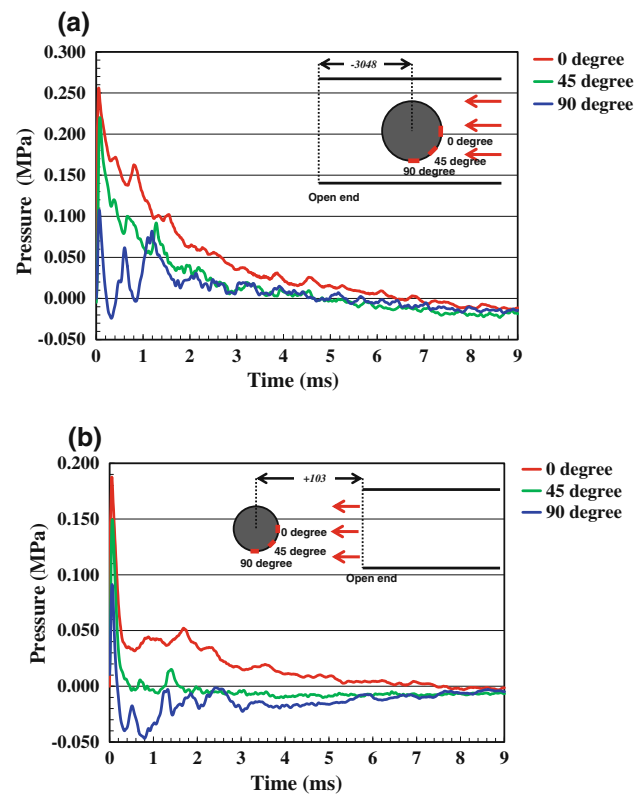

Fig. 9 **a** Experimental p–t profile at various orientations for cylinder placement location of 3048 mm inside the shock tube ($x = -3048$ mm). **b** Experimental p–t profile at various orientations for cylinder placement location of 103 mm outside the shock tube ($x = 103$ mm)

4.3 Pressure profiles at various orientations

Figure 9a shows the pressure profiles for three orientations (0°, 45° and 90°) for cylinder placement location of 3048 mm inside the shock tube. The 0° and 45° orientation shows gradual pressure decay, but the 90° orientation shows flow separation from the cylinder causing a negative pressure phase. This negative phase cannot be sustained and the pressure profile oscillates twice before semi-equilibrating around the other profiles. The 0° orientation experiences the highest pressure because of the kinetic energy contribution from the reflected pressure. Figure 9b shows the pressure profiles for three orientations (0°, 45° and 90°) for cylinder placement location of 103 mm outside the shock tube. All three orientations show a rapid pressure drop after the peak pressure. As mentioned earlier, 0° orientation experiences subsonic jet flow after the rapid pressure decay. For the 45° orientation pressure drops to zero with a slight vacuum. The 90° orientation exhibits flow separation and oscillation, but the pressure mainly remains negative (i.e. negative phase is sustained) due to the lack of shock tube lateral constraints.

For the IED explosions in the intermediate- to far-field range, positive phase durations are much larger than blast
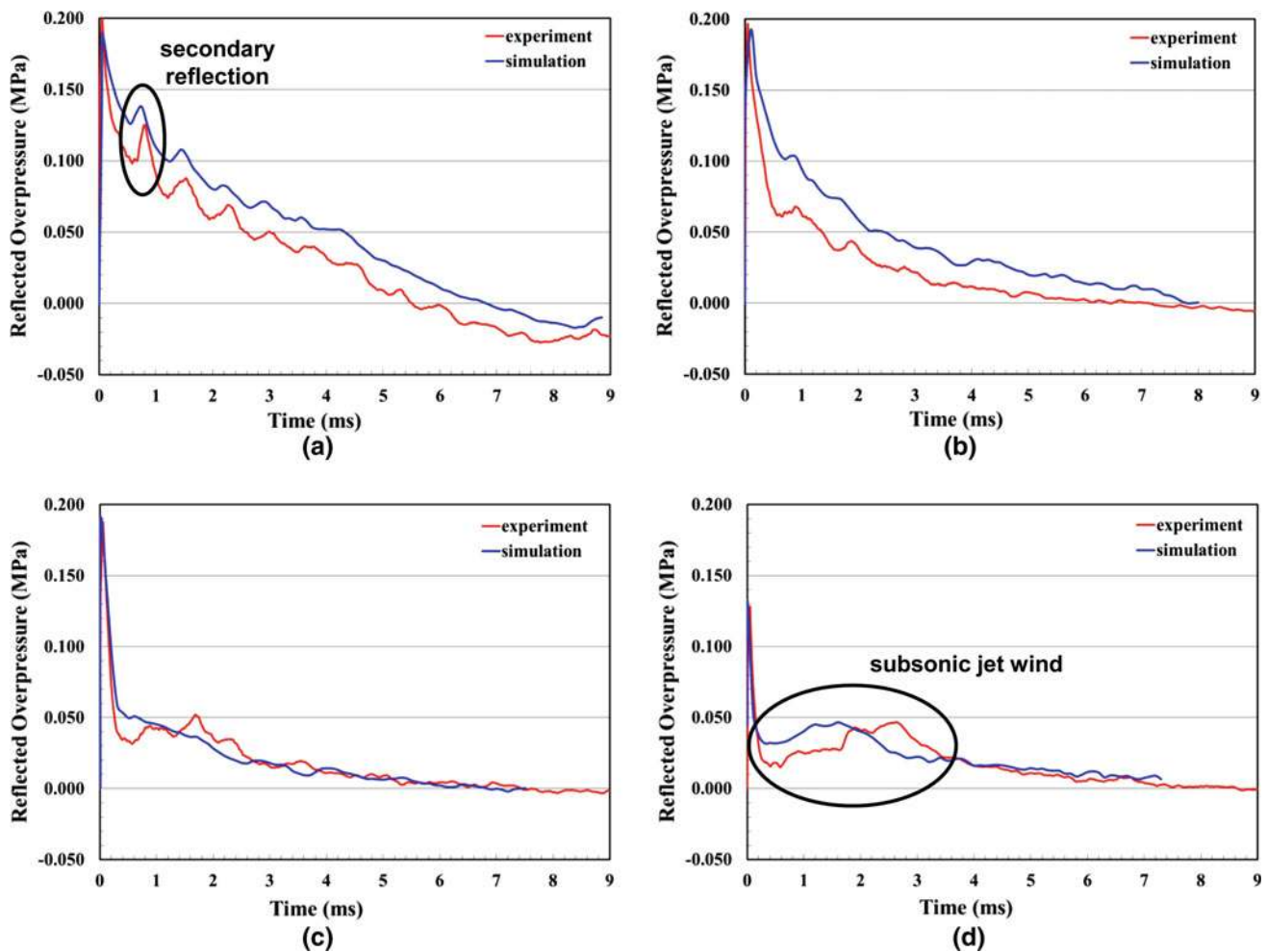
Fig. 10 Comparison of pressure time history from experiments and simulations for sensor t0 for various cylinder placement locations inside and outside of shock tube: **a** $x = -566$ mm; **b** $x = 26$ mm; **c** $x = 103$; **d** $x = 229$

wave traversal time across human head. Thus pressures on the head become relatively uniform as the blast wave traverses the head [30]. Orientation results at 90° outside the shock tube mainly contain tensile loading (negative pressures); this implies that while the front (of the cylinder) is under compression (pushed) the side (of the cylinder) is under tension (i.e. pulled out); this loading pattern is uncharacteristic of IED blasts in the intermediate- to far-field range.

4.4 Comparison of experiments and numerical simulations

Figure 10 shows the pressure–time (p–t) profiles from the shock tube experiments and numerical simulations for sensor t0 for cylinder placement locations inside (566 mm) and outside (26, 103 and 229 mm) of the shock tube. These distances (inside and outside) correspond to possible placements of specimens in experiments; further, these data are also used to analyze for trends and to compare with numerical results. The inside locations correspond to distances, where side-on pressure sensors were already mounted. There is good agree-

ment between the experiments and numerical simulations in terms of peak overpressures, nonlinear decay and positive phase durations which is also evident from Table 1. In general, pressure decay from experiments is faster than that of simulations. The simulations are able to capture majority of the features well, including the shock front rise time, secondary reflections and subsonic jet wind. The arrival of shock wave at sensor t0 from both experiments and simulations is set to zero for ease of comparison of different features of the pressure–time (p–t) profile. There is a slight difference in arrival times between the experiments and the simulations of the order of 0.3 ms, at most. Difference in arrival time indicates difference in shock wave speed and does not change the pressure and impulse experienced by the cylinder. The difference in arrival time between experiments and simulations can be attributed to the ideal gas equation of state modeling assumption, membrane rupture pattern, friction along the inner wall of the shock tube and misinterpretation of the vibrations of the shock tube itself as pressure readings by the pressure sensors [28]. The structural design at UNL is

Table 1 Comparison of peak overpressures and positive phase durations from experiments and simulations

Cylinder placement location (mm)	Peak overpressure (MPa)			Positive phase duration (ms)		
	Experiment	Simulation	% Difference	Experiment	Simulation	% Difference
$x = -566$	0.201	0.189	6.09	5.45	6.75	23.85
$x = 26$	0.198	0.192	3.03	6.06	7.7	27.06
$x = 103$	0.188	0.186	0.88	6.67	6.81	2.10
$x = 229$	0.128	0.133	3.77	–	–	–

made extra stiff by the use of 0.5 in steel plates and reinforcing the structure with stiffeners every 18 inches to avoid vibrations. Zhu et al. [31] also found similar differences in arrival times from their experiments and numerical simulations due to the reasons stated above. The similar agreement in pressure–time (p–t) profiles is observed at other cylinder placement locations and for all other sensors (not shown for brevity).

4.5 Flow field at the exit of the shock tube

Flow field at the exit of the shock tube is studied using numerical simulations. No cylinder case is used to study/demonstrate the flow field at the exit that is free from any artifacts created by the cylinder. Figure 11 shows the pressure and velocity (vector) fields at the exit of the shock tube (no cylinder case). As the blast wave exits the shock tube, the flow changes from planar to three-dimensional spherical (Fig. 11a). Rarefaction wave and vorticities at the corners mix with blast and remaining air ejects as subsonic jet wind, which is evident from velocity vector field of Fig. 11b. This jet wind effect is not present deep inside tube. Further, to clearly demonstrate this, Fig. 12 shows the nodal velocities at various locations inside and outside the shock tube. Since fixed Eulerian mesh is used for modeling, velocity at a given mesh node corresponds to the instantaneous velocity of the material point coincident at given time 't' with the considered node. High-velocity jet wind is recorded in nodal history for locations outside the shock tube. Particle velocity associated with this jet is higher than particle velocity associated with the shock (Fig. 12b). Locations inside the shock tube that are close to the exit also show second peak in velocity due to rarefaction wave moving into the tube, but magnitude of this second peak is lower than particle velocity associated with the jet for outside locations. In addition, magnitude of this second peak gradually reduces as we move inside the shock tube away from the exit (open end). Deep inside the shock tube ($x = -3048$ mm) second peak is completely absent.

To clearly exhibit transition of blast wave from planar to three-dimensional spherical, Fig. 13 shows the pressure distribution at the exit of the shock tube for sequence of times. The black arrows indicate the (velocity) vector field. In each figure outer red contour indicates the primary shock wave

and inner green portion indicates primary vortex loop. The primary shock wave at first appears to be square shaped with rounded corners as shown in Fig. 13i. These corners become significantly rounded and straight parts at the shock tube walls are shortened (Fig. 13ii, iii, iv). This indicates that the primary shock wave is planar at the exit (open end) of the shock tube and evolves three-dimensionally into spherical one as time elapses. This process is called as shock wave diffraction that affects the flow expansion behind it [23]. Similar arguments can be used to show the three-dimensional nature of primary vortex loop which is evident from green color of Fig. 13.

4.6 Flow field evolution for other conditions

The current experiments and simulations were carried out for a long square shock tube with Nitrogen as the driver gas and air as the driven (working) fluid. The evolution of flow field near the exit from planar to three-dimensional, decreasing peak overpressure, conversion from static to kinetic energy and the presence of jet winds are all governed by the physics of the problem. Though this paper addresses a tube with square section, similar flow structure will occur for circular driven tubes, though the structure will be radially symmetric. For larger squares (e.g. 711 mm by 711 mm), the same trends as reported here are observed in computational models.

This study focused on the use of Nitrogen as a driver gas. If Helium is used as the driver gas for the same burst pressure, the shocked air will experience a higher over pressure compared with when Nitrogen is used as the gas. This occurs since the acoustic velocity of the Helium is 965 m/s compared with that of Nitrogen at 334 m/s. However, the overpressure duration in Helium-driven air will be lower than that of nitrogen due to the fact the molecular weight of He is 0.004 kg/mol compared with nitrogen at 0.028 kg/mol. Thus the flow field outside will experience a sharper fall-off in pressure in He-driven cases. In summary, when He is used as the driver gas the physics of the flow field still remains the same except the magnitude and duration will be different.

The effect of driver gas (e.g. compression-driven, explosion, combustible fluid) may alter the flow dynamics both inside and outside of the shock tube. This paper addresses

Fig. 11 **a** Pressure field near the exit of the shock tube. Three-dimensional expansion of shock wave along with vortex formation is seen at the exit. **b** Velocity vector field near the exit of the shock tube. Jet wind is clearly visible in velocity vector field. Representative vector field is shown; jet is also observed at other locations close to the exit at earlier times
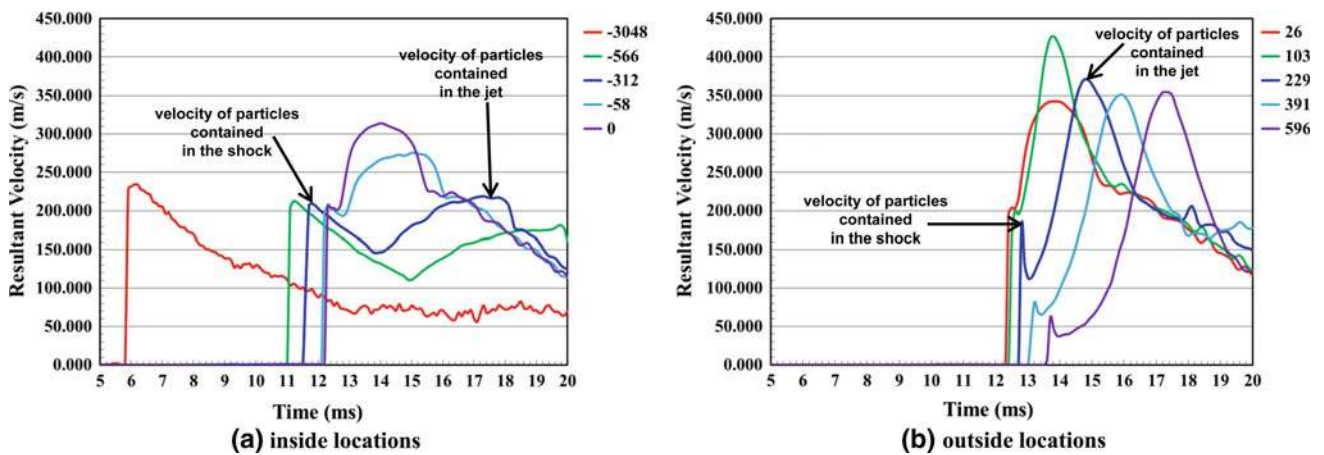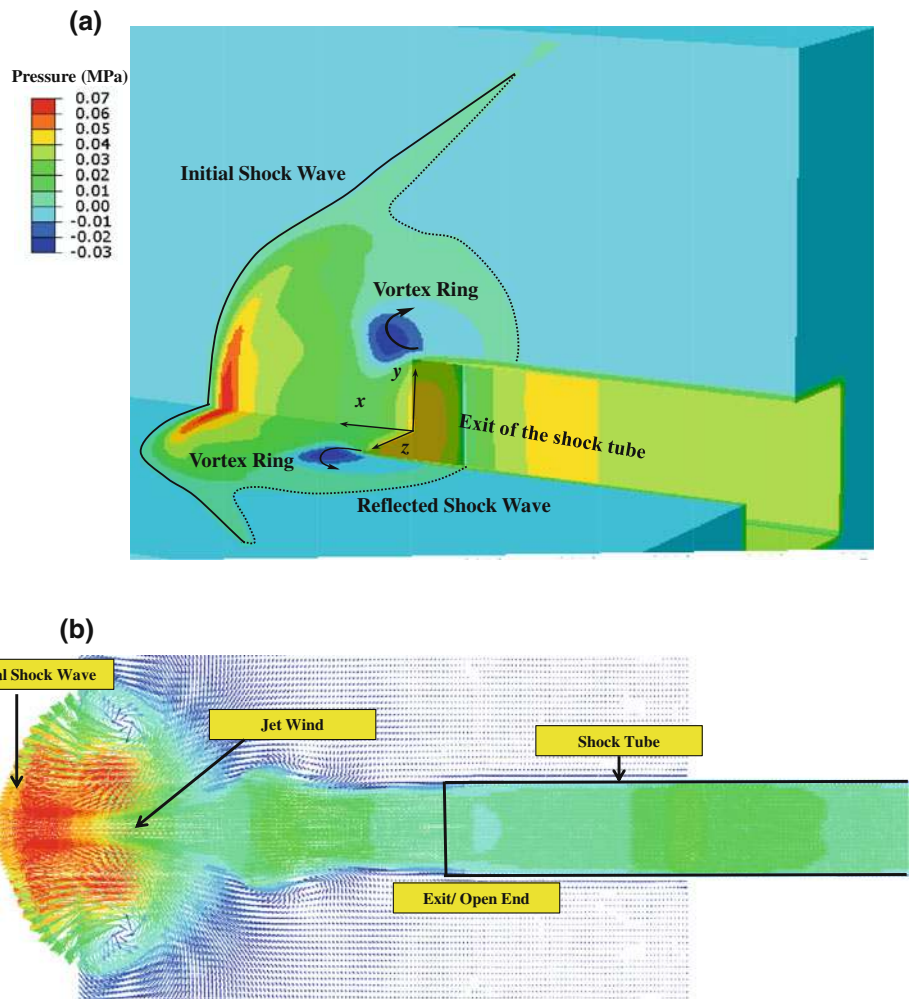

Fig. 12 Nodal velocities at various locations inside and outside the shock tube. Since fixed Eulerian mesh is used for modeling, velocity at a given mesh node corresponds to the instantaneous velocity of the material point coincident at given time '*t*' with the considered node

the issues related to the most-often used compression-driven air shock tubes. The jet wind at the exit develops due to the conversion of potential to kinetic energy in the vicinity of shock exit due to tensile rarefaction wave; how and if this conversion occurs in non-compression-driven shock tubes requires a separate study.

Fig. 13 Flow fields illustrating physics of shock wave diffraction. *Row 1* shows the axial view and *row 2* shows the top view. Arrival of shock wave at the exit is marked as $t = 0$
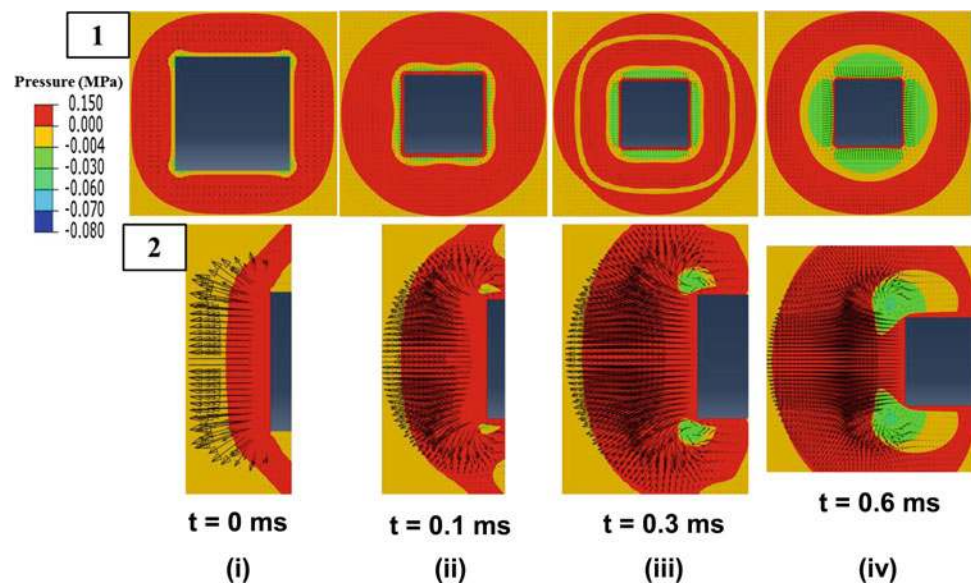
5 Summary and conclusions

Shock tubes have been effectively used in the past to generate explosion type loading. In the event of BINT a key question is how to best replicate the field conditions in controlled and repeatable manner. This study has presented the evolution of blast wave at various locations along the length of the compression-driven air shock tube. Some of the key findings of this work are

- Pressure profiles inside the shock tube follow the Friedlander waveform fairly closely. For locations very close to exit (but inside) the pressure profile is affected by rarefaction wave from the exit. For our shock tube design, optimal pressure profile with minimum artifacts is obtained deep inside the shock tube which happens to be approximately equidistant from the driver and exit (open end) of the shock tube. This location is considered as the best location to conduct BTBI/BINT studies.

- Upon approaching the exit of a shock tube, an expansion wave significantly degrades the measured pressure profiles. The peak pressures and shape of the pressure profiles significantly change with distance from the exit of the shock tube.

- As the blast wave degrades, the remaining flow is ejected as subsonic jet wind.

- A blast wave becomes increasingly non-planar with distance from the exit of a shock tube until it reaches a maximum value and at further distances approaches planarity but with much reduced pressures.

- 90° cylinder orientation shows flow separation. For cylinder placement locations deep inside the shock tube, this flow separation is not sustained but for cylinder placement locations outside the shock tube this flow separation

is sustained which induces tensile loading on the sides of the cylinder that is not typical of loading pattern induced by an IED explosion.

- Results from numerical simulations visually indicate the presence of vortices and jet wind of a blast wave upon exiting the shock tube. In addition, nodal velocity histories confirm that particle velocity associated with the jet wind is higher than particle velocity associated with the shock blast.

- Based on these measurements, it is suggested that caution should be used when testing samples outside of the shock tube because of the non-uniformity of the loading in this region and since the majority of the loading comes from subsonic jet wind which is not part of IED blasts.

References

1. Warden, D.: Military TBI during the Iraq and Afghanistan wars. J. Head Trauma Rehabil. **21**(5), 398–402 (2006)
2. Elder, G.A., Cristian, A.: Blast-related mild traumatic brain injury: mechanisms of injury and impact on clinical care. Mt. Sinai J. Med. **76**(2), 111–118 (2009). doi:10.1002/msj.20098
3. Abdul-Wahab, R., Swietek, B., Mina, S., Sampath, S., Santhakumar, V., Pfister, B.J.: Precisely controllable traumatic brain injury devices for rodent models. In: 2011 IEEE 37th Annual Northeast Bioengineering Conference (NEBEC), pp. 1–2, 1–3 April 2011
4. Alley, M.D., Schimizze, B.R., Son, S.F.: Experimental modeling of explosive blast-related traumatic brain injuries. Neuro-Image **54**(Supplement 1), S45–S54 (2011). doi:10.1016/j.neuroimage.2010.05.030

5. Bolander, R., Mathie, B., Bir, C., Ritzel, D., VandeVord, P.: Skull flexure as a contributing factor in the mechanism of injury in the rat when exposed to a shock wave. Ann. Biomed. Eng. **1**(10), 1–10 (2011). doi:10.1007/s10439-011-0343-0

6. Cernak, I., Wang, Z., Jiang, J., Bian, X., Savic, J.: Cognitive deficits following blast injury-induced neurotrauma: possible involvement of nitric oxide. Brain Injury **15**(7), 593–612 (2001)

7. Chavko, M., Koller, W.A., Prusaczyk, W.K., McCarron, R.M.: Measurement of blast wave by a miniature fiber optic pressure transducer in the rat brain. J. Neurosci. Methods **159**(2), 277–281 (2007). doi:10.1016/j.neumeth.2006.07.018

8. Cheng, J., Gu, J., Ma, Y., Yang, T., Kuang, Y., Li, B., Kang, J.: Development of a rat model for studying blast-induced traumatic brain injury. J. Neurol. Sci. **294**(1–2), 23–28 (2010). doi:10.1016/j.jns.2010.04.010

9. Desmoulin, G.T., Dionne, J.P.: Blast-induced neurotrauma: surrogate use, loading mechanisms, and cellular responses. J. Trauma **67**(5), 1113–1122. doi:1110.1097/TA.1110b1013e3181bb1118e1184 (2009)

10. Ganpule, S., Gu, L., Alai, A., Chandra, N.: Role of helmet in the mechanics of shock wave propagation under blast loading conditions. Comput. Methods Biomech. Biomed. Eng. 1–12 (2011). doi:10.1080/10255842.2011.597353

11. Long, J.B., Bentley, T.L., Wessner, K.A., Cerone, C., Sweeney, S., Bauman, R.A.: Blast overpressure in rats: recreating a battlefield injury in the laboratory. J Neurotrauma **26**(6), 827–840 (2009). doi:10.1089/neu.2008.0748

12. Rafaels, K.: Blast brain injury risk. PhD dissertation, University of Virginia (2010)

13. Saljo, A., Bolouri, H., Mayorga, M., Svensson, B., Hamberger, A.: Low-level blast raises intracranial pressure and impairs cognitive function in rats: prophylaxis with processed cereal feed. J Neurotrauma **27**(2), 383–389 (2010). doi:10.1089/neu.2009.1053

14. Säljö, A., Mayorga, M., Bolouri, H., Svensson, B., Hamberger, A.: Mechanisms and pathophysiology of the low-level blast brain injury in animal models. NeuroImage **54**(Supplement 1), S83–S88 (2011). doi:10.1016/j.neuroimage.2010.05.050

15. Rafaels, K.A., Shridharani, J., Bass, C.R., Salzar, R.S., Walilko, T.J., Panzer, M.B.: Blast wave attenuation: ballistic protective helmets and the head. Paper presented at the Personal Armor Safety Symposium (PASS), Washington, DC (2010)

16. Duff, R.E., Blackwell, A.N.: Explosive driven shock tubes. Rev Sci Instrum **37**(5), 579–586 (1966)

17. Courtney, A.C., Andrusiv, L.P., Courtney, M.W.: Oxy-acetylene driven laboratory scale shock tubes for studying blast wave effects. Rev. Sci. Instrum. **83**(4) (2012). doi:10.1063/1.3702803

18. Bleakney, W., Taub, A.H.: Interaction of shock waves. Rev. Mod. Phys. **21**(4), 584–605 (1949)

19. Baker, W.E.: Explosions in air. University of Texas Press, Texas (1973)

20. Arakeri, J.H., Das, D., Krothapalli, A., Lourenco, L.: Vortex ring formation at the open end of a shock tube: a particle image velocimetry study. Phys. Fluids **16**(4), 1008–1019 (2004). doi:10.1063/1.1649339

21. Honma, H., Ishihara, M., Yoshimura, T., Maeno, K., Morioka, T.: Interferometric CT measurement of three-dimensional flow phenomena on shock waves and vortices discharged from open ends. Shock Waves **13**(3), 179–190 (2003). doi:10.1007/s00493-003-0206-1

22. Jiang, Z., Onodera, O., Takayama, K.: Evolution of shock waves and the primary vortex loop discharged from a square cross-sectional tube. Shock Waves **9**(1), 1–10 (1999). doi:10.1007/s001930050133

23. Jiang, Z., Wang, C., Miura, Y., Takayama, K.: Three-dimensional propagation of the transmitted shock wave in a square cross-sectional chamber. Shock Waves **13**(2), 103–111 (2003). doi:10.1007/s00193-003-0197-y

24. Kashimura, H., Yasunobu, T., Nakayama, H., Setoguchi, T., Matsuo, K.: Discharge of a shock wave from an open end of a tube. J. Therm. Sci. **9**(1), 30–36 (2000). doi:10.1007/s11630-000-0042-x

25. Onodera, O., Jiang, Z.L., Takayama, K.: Holographic interferometric observation of shock waves discharged from an open-end of a square cross-sectional shock tube. JSME Int. J. Ser. B: Fluids Therm. Eng. **41**(2), 408–415 (1998)

26. Setoguchi, T., Matsuo, K., Hidaka, F., Kaneko, K.: Impulsive noise induced by a weak shock wave discharged from an open end of a tube: acoustic characteristics and its passive control. In: Proceedings of the 1993 ASME Winter Meeting, November 28–December 3, 1993, New Orleans, LA, USA, 1993. American Society of Mechanical Engineers, Fluids Engineering Division (Publication) FED, pp. 57–64. ASME

27. Chandra, N., Holmberg, A., Feng, R.: Controlling the shape of the shock wave profile in a blast facility. U.S. Provisional patent application no. 61542354 (2011)

28. Jiang, Z., Takayama, K., Skews, B.W.: Numerical study on blast flowfields induced by supersonic projectiles discharged from shock tubes. Phys. Fluids **10**(1), 277–288 (1998). doi:10.1063/1.869566

29. Kleinschmit, N.N.: A Shock Tube Technique for Blast Wave Simulation and Studies of Flow Structure Interactions in Shock Tube Blast Experiments. University of Nebraska-Lincoln, Lincoln (2011)

30. Moss, W.C., King, M.J., Blackman, E.G.: Distinguishing realistic military blasts from firecrackers in mitigation studies of blast-induced traumatic brain injury. Proc. Natl. Acad. Sci. USA **108**(17), E82–E82 (2011). doi:10.1073/pnas.1101671108

31. Zhu, F., Wagner, C., Dal Cengio Leonardi, A., Jin, X., Vande Vord, P., Chou, C., Yang, K., King, A.: Using a gel/plastic surrogate to study the biomechanical response of the head under air shock loading: a combined experimental and numerical investigation. Biomech. Model. Mechanobiol. 1–13. doi:10.1007/s10237-011-0314-2